ACS Energy LETTERS

http://pubs.acs.org/journal/aelccp

Superstable Small-Molecule Quinone Cathode Enabled by Host–Guest Interactions for Fast-Kinetics Zinc-Organic Batteries at Low Temperature

Published as part of ACS Energy Letters special issue "Celebrating 10 Years of the Collaborative Innovation Center of Chemistry for Energy Materials (iChEM)".

Jin Yang, Rong Tang, Yuanhong Kang, Minghao Zhang, Guanhong Chen, Zeheng Lv, Zhipeng Wen, Cheng Chao Li, Yang Yang,* and Jinbao Zhao*

Cite This: ACS Energy Lett. 2024, 9, 4598–4606

ABSTRACT: Aqueous zinc-organic batteries, featuring safe aqueous electrolytes and cost-effective materials, demonstrate broad application prospects. However, small-molecule organic cathodes encounter critical challenges, including poor electronic conductivity and severe dissolution issues. Herein, a small-molecule quinone guest (sodium anthraquinone-2-sulfonaterationate, SAS) is incorporated with a conductive host (reduced graphene oxide, rGO) through noncovalent bonding to obtain a free-standing SAS@rGO electrode. Theoretical calculations and experimental characterizations indicate host–guest interactions prevent the dissolution of active material and facilitate electron transport. Furthermore, various in/ex situ characterizations reveal that SAS@rGO remains stable during cycling, maintaining a high capacity retention of 90.4% after 300 cycles even at 0.5 C. Moreover, 1,4-butyrolactone is adopted as cosolvent to break the hydrogen bonding network, ensuring rapid ion transport kinetics at low temperatures. Combining the principles of host–guest and solvation chemistry synergistically, the Zn//SAS@rGO battery achieves exceptional cycling stability for over 3000 cycles at 1 A g^{-1} and −40 °C.

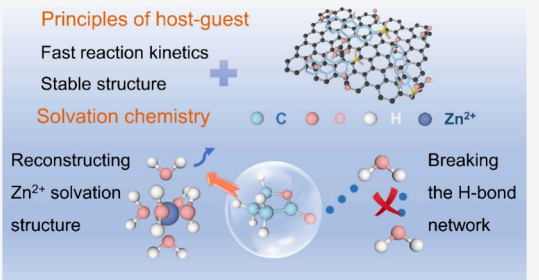

Due to high theoretical capacity (820 mAh g^{-1}), suitable redox potential (−0.76 V vs standard hydrogen electrode), affordability ($1.45/lb), and the intrinsic safety of zinc, aqueous zinc-ion batteries (ZIBs) have emerged as prominent alternatives in stationary energy storage.[1−8] However, widely studied inorganic cathode materials (such as V_2O_5, MnO_2, and Prussian blue analogues) frequently encounter issues related to resource availability, environmental impact, and compromised electrode structural stability caused by the (de)intercalation of bivalent Zn^{2+}. In contrast, organic cathodes consist of abundant natural elements such as C, H, O, and N, ensuring their resource renewability, environmental sustainability, and structural design flexibility. Furthermore, they undergo only chemical bond rearrangements during the redox process, effectively circumventing structural collapse.[9−12]

Among various types of organic cathodes, carbonyl compounds have garnered significant attention for their high specific capacity, excellent redox reversibility, and cost-effective raw materials.[13−19] However, organic carbonyl compounds, mostly small-molecule quinones, may face severe dissolution issues in water. Traditional polymerization synthesis modifications can be cumbersome and may introduce inactive groups, resulting in a reduced specific capacity. Additionally, their limited electronic conductivity often necessitates the addition of substantial amounts of conductive carbon agents. Notably, Wang and Li et al. pioneered an approach by combining small carbonyl molecules with highly conductive graphene, forming an integrated xerogel electrode for enhanced electrochemical performance in supercapacitors.[20]

Received: June 25, 2024
Revised: August 21, 2024
Accepted: August 22, 2024
Published: August 27, 2024

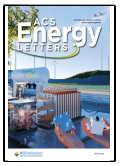

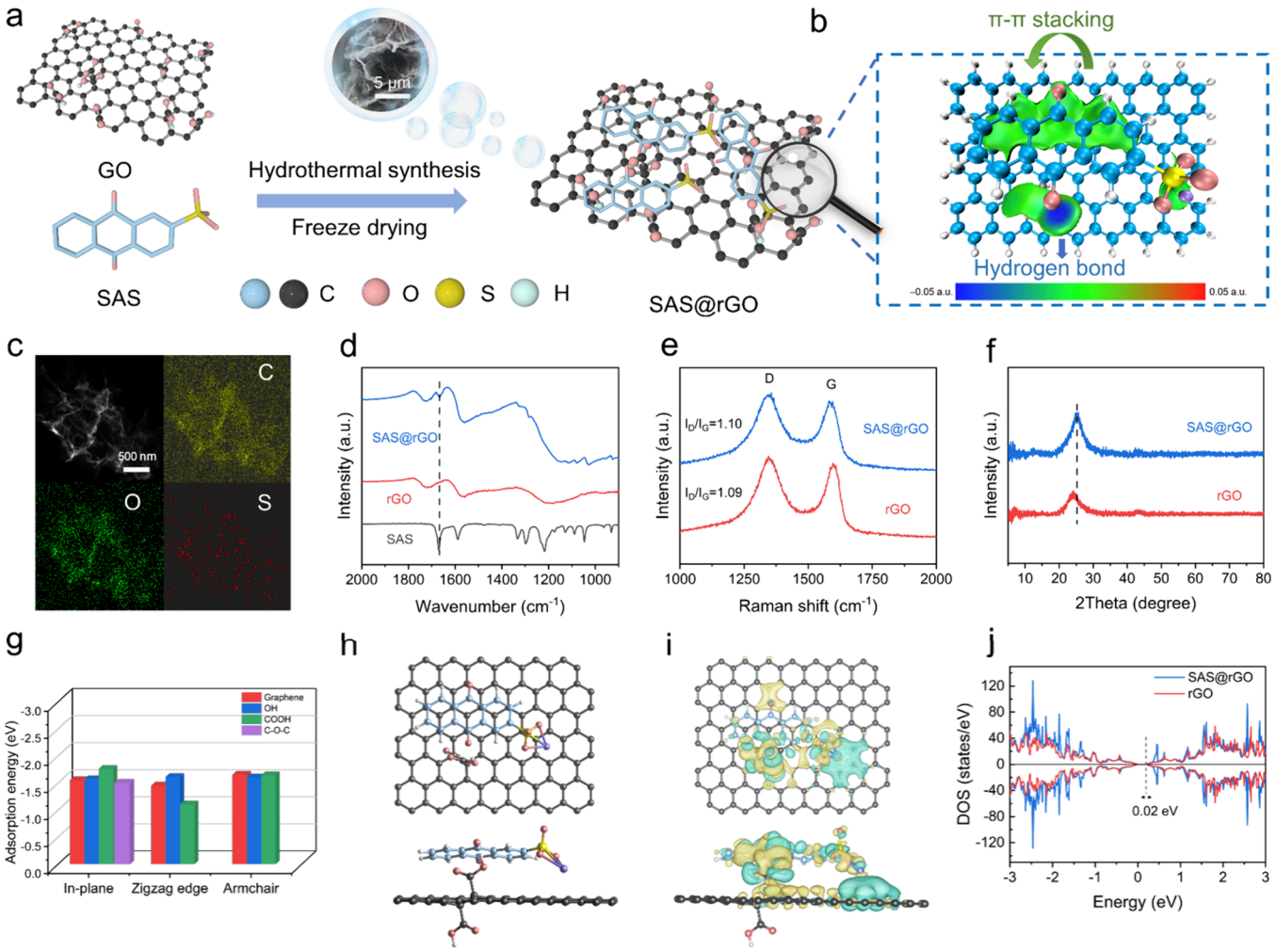

Figure 1. (a) Schematic diagram of the synthesis and SEM pictures of SAS@rGO. (b) Sign(λ_2)ρ colored isosurface of δg^{inter} = 0.003 au of SAS@rGO corresponding to IGMH analyses. (c) TEM images and EDS mapping of SAS@rGO. (d) FTIR spectra of SAS@rGO, SAS, and rGO. (e) Raman spectra and (f) XRD characterization of SAS@rGO and rGO. (g) Adsorption energies of SAS on rGO surfaces modified by various functional groups. (h) Optimized geometries of SAS with −COOH on the in-plane rGO surface. (i) Charge density differences of (h). (j) DOS of SAS@rGO and rGO.

On the other hand, operating aqueous ZIBs in cold regions is also a significant challenge for practical applications. While organic cathodes offer excellent redox kinetics, not relying on sluggish ion diffusion in crystalline hosts, the increased charge-transfer impedance in the electrolyte and Zn anode at low temperatures can be detrimental. Therefore, the development of both stable organic cathodes and low-temperature electrolytes is foreseeable for achieving high-performance organic ZIBs with robust low-temperature tolerance.[21−24]

Host−guest chemistry is a fundamental concept in modern supramolecular chemistry, which involves the binding of a host molecule to a guest molecule through forces other than full covalent bonds. This has inspired us to design small-molecule quinones based on the principles of molecular recognition. Herein, we rationally designed a conductive host (reduced graphene oxide, rGO) that binds with a small-molecule guest (sodium anthraquinone-2-sulfonate, SAS) through noncovalent bonding, forming a self-standing electrode that eliminates the need for additional conductive agents and binders. Diverging from conventional physical mixing methods, the chemical $\pi-\pi$ stacking and hydrogen bond interactions between SAS and rGO not only impede material dissolution but also enhance electron transport through electron coupling. Consequently, this approach achieves exceptional cycling stability, even at low current densities. Moreover, 1,4-butyrolactone (1,4-BL) was chosen as a cosolvent to break the hydrogen bonding network of H_2O molecules, enhancing the Zn anode reversibility at low temperature.

The SAS@rGO composite cathode was synthesized via a facile one-step reaction (Figure 1a). The scanning electron microscopy (SEM) image shows that the synthesized material exhibits a typical porous structure at the micrometer level, facilitating electrolyte wetting and ion transmission. An independent gradient model based on Hirshfeld partition (IGMH) analyses[25,26] further revealed the interaction between SAS and rGO (Figures 1b and S1). The green surface between the two layers signifies extensive $\pi-\pi$ stacking. Additionally, clear hydrogen bonds are present between the carbonyl group on rGO and the carboxyl group on SAS, as indicated by the blue surface. These host−guest interactions are expected to inhibit material dissolution effectively, which was confirmed by an ultraviolet visible (UV−vis) absorption spectrum (Figure S2). The transmission electron microscopy (TEM) image reveals a thin, plate-like morphology, and energy dispersive

https://doi.org/10.1021/acsenergylett.4c01692
ACS Energy Lett. 2024, 9, 4598−4606

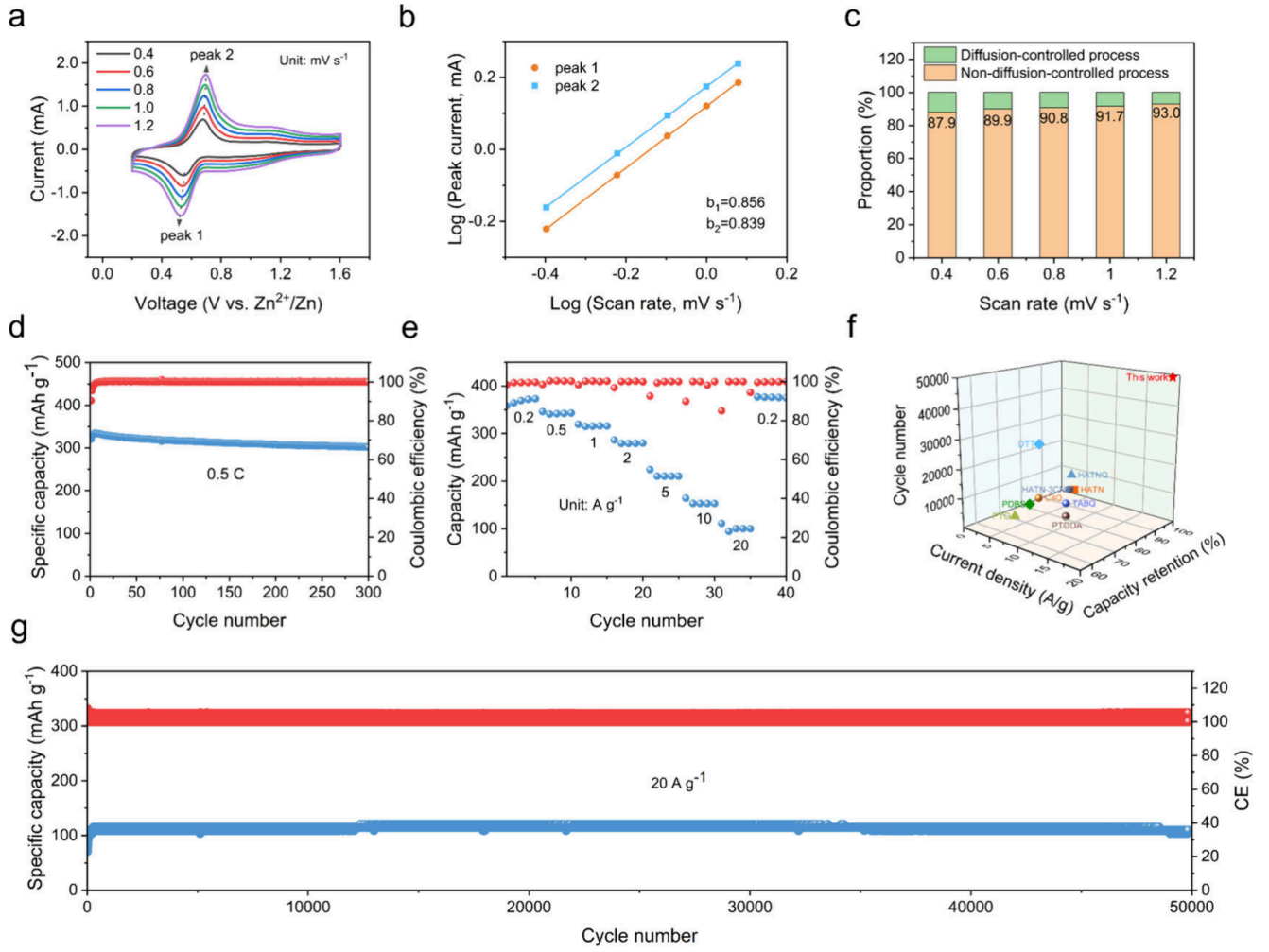

Figure 2. (a) CV curves of SAS@rGO at different scan rates. (b) Plots of log (peak current, mA) versus log (scan rate, mV s^{-1}) using the corresponding peak current and the scan rate in the CV curves of SAS@rGO at different scan rates. (c) Diffusion-controlled process and nondiffusion-controlled capacity contributions at different scan rates. (d) Cycling stability at a low current density of 0.5 C. (e) Rate performance of SAS@rGO at various current densities. (f) Cycle performance comparison of SAS@rGO cathode with representative reported organic cathodes. (g) Long-term cycling stability of Zn//SAS@rGO batteries.

spectroscopy (EDS) mapping confirms the uniform distribution of C, O, and S elements (Figure 1c). The Fourier-transform infrared (FTIR) characteristic peaks of SAS (C═O) are retained in that of SAS@rGO, and the peak at 1589 cm^{-1} attributed to the C═C vibrations in SAS shifts to 1561 cm^{-1} in SAS@rGO (Figure 1d), which contributes to the weakening of the C═C characteristics on the benzene ring due to $\pi-\pi$ stacking interactions. Furthermore, both SAS@rGO and rGO exhibit two similar peaks at 1348 and 1598 cm^{-1} in Raman spectra (Figure 1e), corresponding to the disorder in the crystal structure (D band) and E_{2g} vibration of sp^2 hybridized carbon atoms (G band), respectively. The similar I_D/I_G values indicate that the introduction of SAS does not increase the degree of disorder in rGO. The XRD pattern of rGO host displays a peak at 2θ = 24.2° attributed to the (002) peak of carbonaceous materials, which shifts slightly to higher angles after the incorporation of SAS guest (Figure 1f), corroborating the intercalation of SAS between rGO interlayers. The content of SAS in SAS@rGO was determined to be ~30% by thermogravimetric (TG) analyses (Figure S3). Furthermore, first-principles calculations were conducted to obtain the adsorption energies between different sites and groups on rGO and SAS (Figures 1g and S4). All adsorption energies fall within the range of −1.1 to 1.8 eV, indicating a strong interaction between rGO and SAS. Notably, when SAS binds with the carbonyl groups on the planar surface of rGO, the binding energy is the highest (Figure 1h), confirming that the aromatic rings of SAS are stacked parallel to those of rGO. Charge density differences were further calculated to explore their interactions (Figure 1i). A notable redistribution of charge takes place within the SAS@rGO, resulting in the establishment of negative and positive centers on the C═O and $-SO_3^-$ groups, thereby fostering the creation of a space charge layer. Therefore, the substantial adsorption energy can be attributed to the combination of $\pi-\pi$ stacking and the space charge layer. More importantly, the space charge layer should facilitate the conduction of electrons during the redox process. During discharging, the C═O group of SAS preferentially receives electrons from the highly conductive rGO host through the space charge layer and then combines with cations near the electrode/electrolyte interface. Besides, the total density of electron states (DOS) for rGO and SAS absorbed on the in-plane rGO surface was also calculated (Figure 1j). It is noteworthy that the latter shows a smaller distance from the

https://doi.org/10.1021/acsenergylett.4c01692
ACS Energy Lett. 2024, 9, 4598−4606

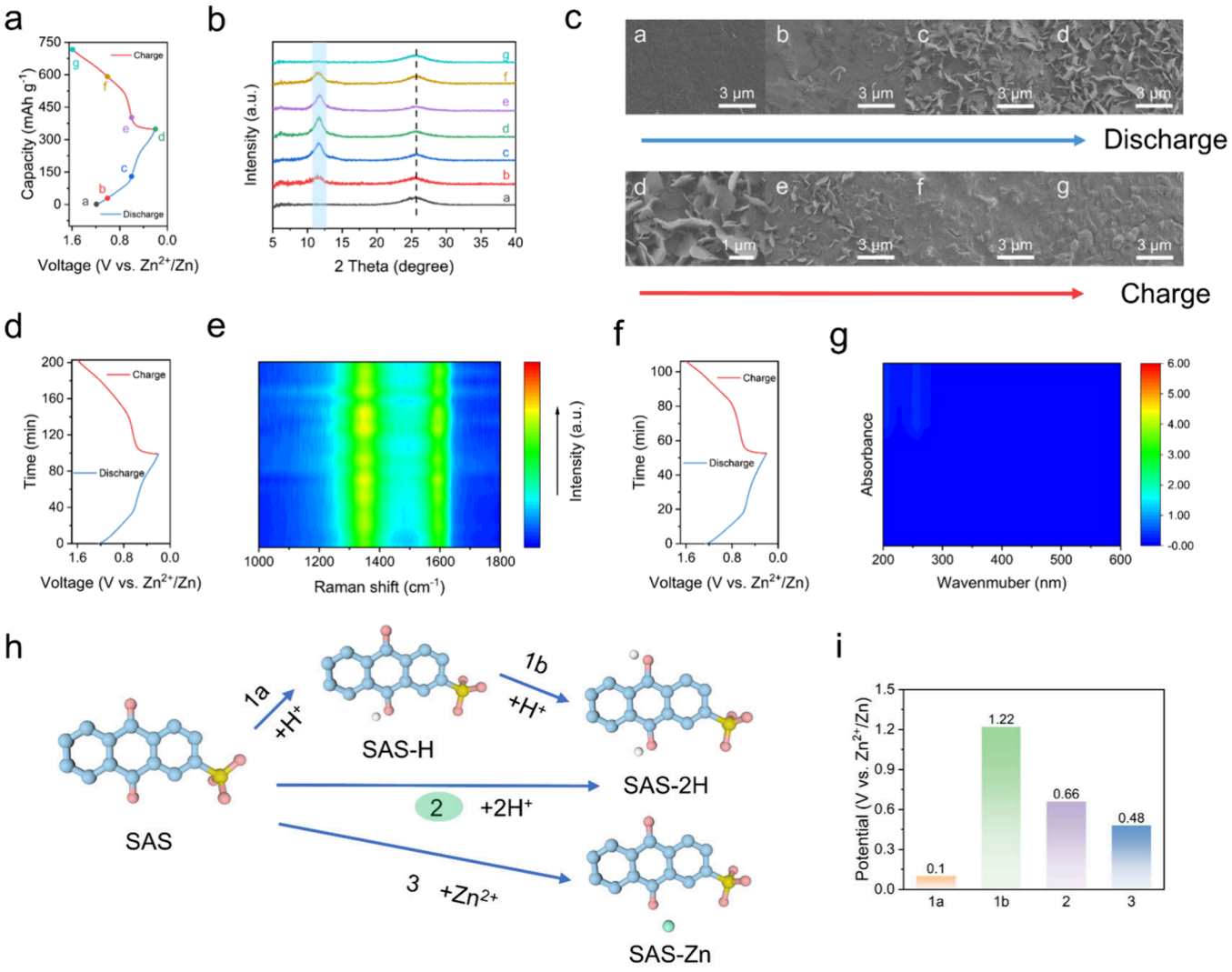

Figure 3. (a) GCD curves of SAS@rGO cathode with different charge−discharge depths. (b) Ex situ XRD patterns, (c) ex situ SEM images, (d, e) in situ Raman spectra, and (f, g) in situ UV−vis absorption spectra of SAS@rGO cathodes. (h) Three pathways of SAS binding to different ions during discharge and (i) corresponding potentials.

Fermi level to the bottom of the conduction band compared to that of rGO alone, confirming the enhanced electronic conductivity of SAS@rGO.

Electrochemical performance was evaluated by Zn//SAS@rGO batteries assembled with a 2 M $ZnSO_4$ aqueous electrolyte. Cyclic voltammetry (CV) curves of the SAS@rGO electrode exhibit a pair of redox peaks at 0.55/0.68 V with a scan rate of 0.2 mV s^{-1}, in agreement with redox behavior of the carbonyl groups in the SAS molecule (C═O ↔ C−O^-) (Figure 2a). Based on the CV curves at different sweep rates, it can be concluded that the slopes of log (peak current) of redox peaks over log (scan rate) are close to 1, implying that capacitance behavior dominates in the charging/discharging processes (Figure 2b). Furthermore, the proportion of nondiffusion-controlled capacity is notably high and gradually increases with the scan rate, contributing to rate performance (Figure 2c). The galvanostatic discharge/charge (GCD) curves reveal that the SAS@rGO electrode exhibits an exceptionally high capacity of ∼360 mAh g^{-1} at 0.2 A g^{-1}, accompanied by a discharge plateau at 0.6 V (Figure S5), while the specific capacity of pure SAS cathode decays to almost 0 mAh g^{-1} after only three cycles due to its inherent high solubility (Figure S6).

It should be noted that the specific capacity of SAS@rGO is denoted as the weight of SAS and the specific capacity of pure rGO was also tested, as shown in Figure S7. As the current density increases as high as 20 A g^{-1}, the SAS@rGO electrode can still maintain a specific capacity up to 111 mAh g^{-1}. And the specific discharge capacity could recover to 376 mAh g^{-1} when the current density is reduced back to 0.2 A g^{-1} (Figure 2e). Moreover, the SAS@rGO electrode exhibits outstanding cycle stability, performing 50,000 cycles with almost no capacity degradation, even under the high current density of 20 A g^{-1} (Figure 2g). Such an ultralong lifespan is superior to many previously reported organic cathode materials (Figure 2f).[27−35] Nevertheless, considering the dissolution issues are even more severe during low-rate cycling, it is crucial to demonstrate cycle stability at the moderate rates (0.25 to 2 C) for ZIBs to meet practical requirements.[36,37] Benefiting from the $\pi-\pi$ stacking interaction that inhibits dissolution, the SAS@rGO electrode exhibited an outstanding cycling stability at a low current density of 0.5 C (e.g., only 0.032% capacity decay per cycle over 300 cycles; Figure 2d), demonstrating its practical potential.

https://doi.org/10.1021/acsenergylett.4c01692
ACS Energy Lett. 2024, 9, 4598−4606

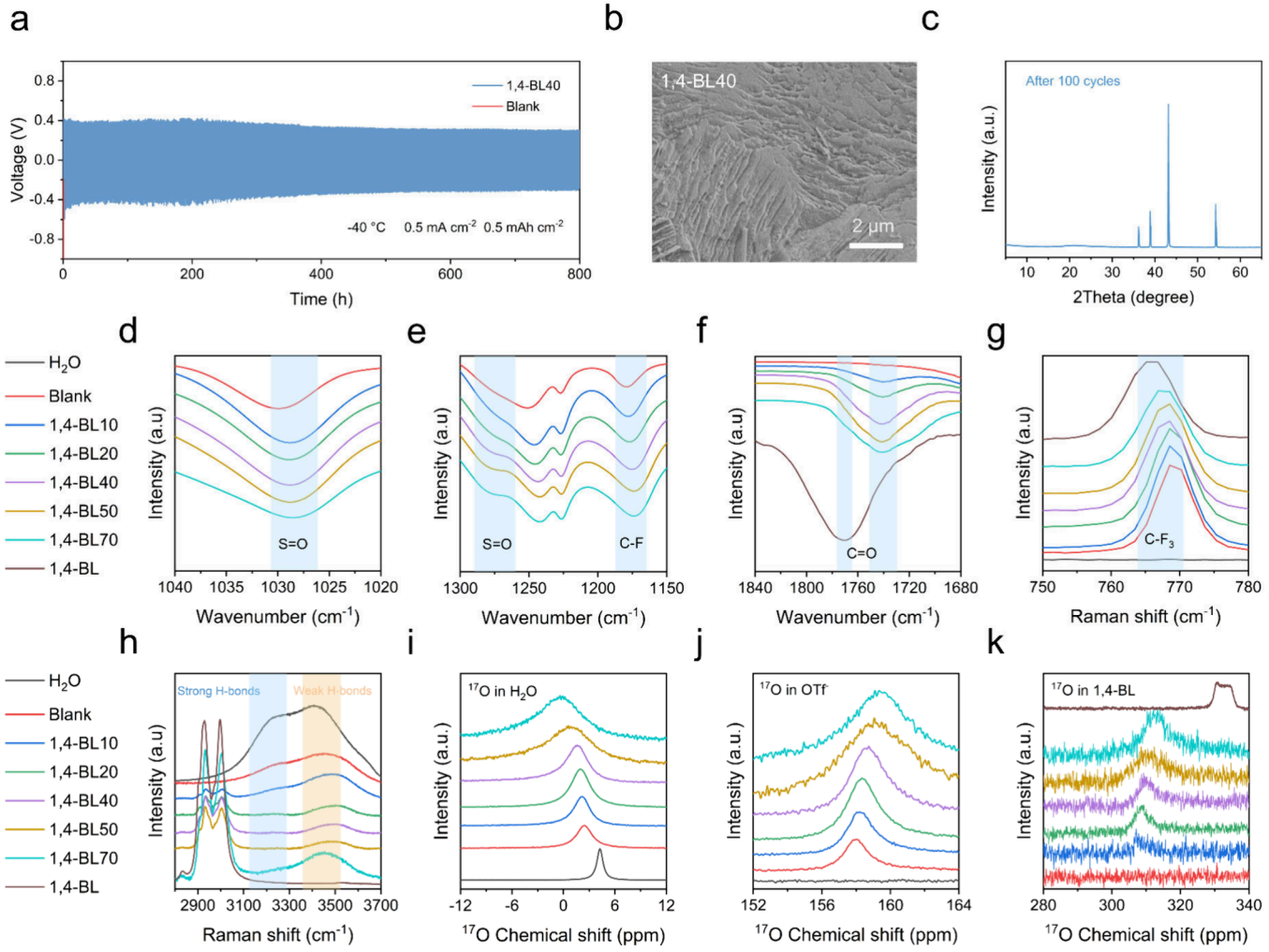

Figure 4. (a) Voltage profiles of Zn//Zn cell with 1,4-BL40 electrolyte at 0.5 mA cm^{-2} for 0.5 mAh cm^{-2}. (b) SEM image and (c) XRD profile of zinc foil after 100 cycles in Zn//Zn cell with 1,4-BL40 electrolyte. (d–f) FTIR spectra, (g, h) Raman spectra, and (i–k) liquid-state NMR spectra of H_2O, 1,4-BL, and hybrid electrolytes.

Various ex situ and in situ characterization methods were employed to verify the structural stability of the SAS@rGO electrode during cycling. Ex situ XRD patterns showed the (002) peak of SAS@rGO remained unchanged during the charge–discharge cycle, indicating that the intercalation and deintercalation of ions did not affect the interlayer spacing of SAS@rGO (Figure 3a,b). The D and G bands did not exhibit significant shift, and the I_D/I_G retained stable throughout the cycle in in situ Raman spectroscopy (Figures 3d,e and S8), confirming the excellent structural stability of SAS@rGO. In situ UV–vis spectroscopy showed weak absorption peak signals corresponding to SAS (Figure 3f,g), and the value of absorbance was further substituted into the UV standard curve to calculate that only 3% of SAS in the SAS@rGO electrode dissolved during the initial cycle (Figure S9). The above in situ and ex situ tests consistently indicate that the structure of SAS@rGO remains intact during cycling, even at a low current density, which aligns with the high capacity retention of SAS@rGO.

Given that H^+/Zn^{2+} cointercalation is known to occur in aqueous electrolytes, it is necessary to explore the energy storage mechanism of SAS@rGO during cycling.[38,39] The periodic formation and disappearance of hydroxide sulfate Zn compounds were detected in ex situ XRD patterns (Figure 3a,b), arising from a local pH change due to proton binding and release from SAS@rGO during cycle. Ex situ SEM images also confirmed the aggregation of flakelike morphologies corresponding to hydroxide sulfate Zn compounds on the surface of SAS@rGO during discharge, which disappeared during the charging process (Figure 3c). Density functional theory (DFT) calculations were undertaken to furnish insightful understanding of the energy storage mechanism of SAS@rGO electrodes. Electrostatic potential (ESP) analysis, showing charge distribution on the surface of SAS, confirmed that C═O is the main active site (Figure S10). The potentials of three pathways of SAS in the discharge process were calculated, respectively (Figure 3h,i), namely, the binding of two protons in succession (pathway 1), the binding of two protons at one time (pathway 2), and the binding of zinc ions (pathway 3). In the case of pathway 1, the calculated potential of pathway 1a is lower than that of pathway 1b, implying that it is not feasible during discharging. On the contrary, the potentials of pathway 2 and pathway 3 are 0.66 and 0.49 V, respectively, suggesting that SAS preferably follows pathway 2 during discharging. Notably, the calculated potential of pathway 2 is also close to the actual discharge platform of SAS@rGO. In summary, the experimental results and theoretical calculations reveal that SAS@rGO preferentially

https://doi.org/10.1021/acsenergylett.4c01692
ACS Energy Lett. 2024, 9, 4598–4606

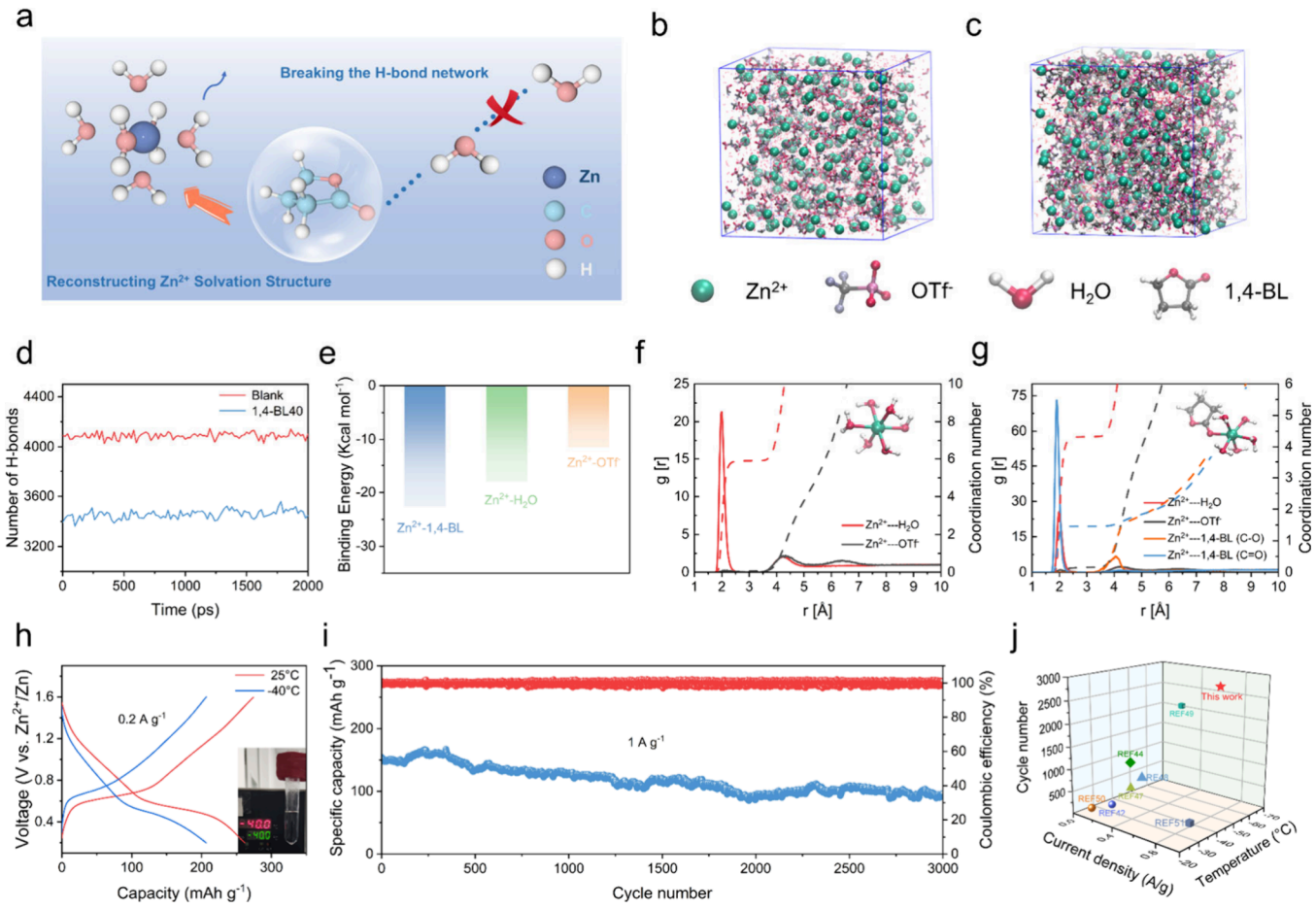

Figure 5. (a) Schematic illustration of the role of 1,4-BL in the hybrid electrolyte. (b, c) MD simulations cells of blank and 1,4-BL40 electrolytes. (d) Number of H-bonds between water molecules of blank and 1,4-BL40 electrolytes. (e) Binding energy for Zn^{2+} with 1,4-BL, H_2O, and OTf^-. (f, g) Corresponding RDF plots for (b, c) (insets are representative solvation structure within a 0.3 nm scale). (h) GCD curves of SAS@rGO cathodes in hybrid electrolyte at 25 °C and −40 °C (inset is optical picture of 1,4-BL40 electrolyte at −40 °C). (i) Cycling performance of Zn//SAS@rGO at −40 °C and current density of 1 A g^{-1}. (j) Performance comparison of Zn//SAS@rGO with other low-temperature ZIBs.

combines with two protons simultaneously during the discharge process, with subsequent proton detachment during the charge process.

Regarding the low-temperature performance of ZIBs, designing an electrolyte that complements the fast reaction kinetics of the SAS@rGO cathode is particularly crucial. 1,4-BL has been extensively employed as an antifreeze due to its high dielectric constant (39 at 25 °C), low viscosity (1.73 cP at 25 °C), and low melting point (−44 °C).[40,41] Besides, a salting-in effect enables $Zn(OTf)_2$ to dissolve in a hybrid electrolyte of organic solvents/water.[24] Consequently, 1,4-BL was introduced as a cosolvent into 3 M $Zn(OTf)_2$ to prepare various hybrid electrolytes: blank, 1,4-BL10, 1,4-BL20, 1,4-BL40, 1,4-BL50, and 1,4-BL70 hybrid electrolytes, where the ratios of water to 1,4-BL were 10:0, 9:1, 8:2, 6:4, 5:5, and 3:7, respectively. All electrolytes are clear and transparent (Figure S11), with suitable viscosities and conductivities (Figures S12 and S13).

The zinc plating/stripping process at −40 °C was first assessed by utilizing Zn//Zn symmetric cells. The symmetric cell employing 1,4-BL40 electrolyte achieved a long lifespan of over 800 h at 0.5 mA cm^{-2} for 0.5 mAh cm^{-2}, whereas the cell with the blank electrolyte fails to work (Figure 4a). The SEM image reveals a compact and uniform lamellar structure of the zinc foil after 100 cycles, (Figure 4b). Besides, there is no peak of basic zinc salt in the XRD profile (Figure 4c). In addition, Zn//Zn symmetric cells with the 1,4-BL40 electrolyte also exhibited stable cycling over 1500 h at room temperature (Figure S14). These results indicate that the 1,4-BL40 hybrid electrolyte is conducive to the uniform deposition of zinc anode and reduces the generation of byproducts, achieving long cycles at low temperatures. To deeply demonstrate the interaction among 1,4-BL, OTf^-, and H_2O, FTIR was conducted to characterize the solvation structure of hybrid electrolytes. The peak located at 1030 cm^{-1}, ascribed to OTf^- in water, gradually red shifts with the increase of 1,4-BL content, indicating changes in the solvation environment of OTf^- (Figure 4d). The same red shift of the $-CF_3$ and SO_3^- groups also verifies this result (Figure 4e). More importantly, for pure 1,4-BL solvent, there is a peak located at 1770 cm^{-1}, corresponding to C═O stretching (Figure 4f), while with the introduction of 1,4-BL, a new peak appears at 1740 cm^{-1}, and the intensity increases with the increase of 1,4-BL content, suggesting the 1,4-BL molecules participate in the coordination of Zn^{2+}. Similar peak changes also occurred in the Raman spectrum (Figures 4g and S15). The O−H stretching vibration peak can be divided into three parts in the 3200−3700 cm^{-1} wavelength range, namely, strong H-bonds at 3230 cm^{-1}, weak

https://doi.org/10.1021/acsenergylett.4c01692
ACS Energy Lett. 2024, 9, 4598−4606

H-bonds at 3450 cm^{-1}, and broken H-bonds at 3620 cm^{-1}.[42,43] As can be seen in Figure 4h, the increased ratios of weak H-bonds to strong H-bonds with the introduction of 1,4-BL confirmed the devastation of the H-bond structure, which is favorable for lowering the freezing point. Liquid NMR was further employed to verify the interaction of Zn^{2+}, OTf^-, H_2O, and 1,4-BL. With the addition of 1,4-BL, the peak of ^{17}O in water broadens and shifts downfield, implying the increased electron density due to the breakdown of the hydrogen-bond network (Figure 4i). In contrast, the peak of ^{17}O in OTf^- and 1,4-BL moved upfield upon addition of 1,4-BL, which is attributed to the reduced concentration of water. (Figure 4j,k). Besides, it can be noted that with the addition of 1,4-BL, the peak of ^{17}O in C═O is significantly shifted while that in C−O remains almost unchanged, confirming that Zn^{2+} ions are mainly coordinated with O in C═O (Figure S16).

Molecular dynamics simulations were conducted on various electrolytes: blank, 1,4-BL40, and 1,4-BL70 (Figures 5b,c and S17a), and radial distribution function (RDF) plots were further employed to analyze the coordination within the solvation shell of Zn^{2+} (Figures 5f,g and S17b). In the absence of 1,4-BL, there was only one peak appearing within 0.3 nm of Zn^{2+} (primary solvation shell), and the corresponding representative solvation structure indicates that Zn^{2+} tends to coordinate with six water molecules rather than OTf^- in the primary solvation shell. After introducing 1,4-BL, the interaction force between Zn^{2+} and water molecules was weakened and the strong interaction force of Zn^{2+}-1,4-BL allowed 1,4-BL to enter the primary solvation shell. Moreover, the number of hydrogen bonds between water molecules in the 1,4-BL40 electrolyte is significantly reduced compared to that of the blank electrolyte (Figure 5d). The binding energies of Zn^{2+}-H_2O, Zn^{2+}-1,4-BL, and Zn^{2+}-OTf^- also confirm that Zn^{2+} is more inclined to bind 1,4-BL instead of H_2O and OTf^- (Figure 5e). Besides, the electrostatic potential of the 1,4-BL-Zn^{2+}-$5H_2O$ solvation state decreases after introducing 1,4-BL into the system, thus reducing the electrostatic repulsion between Zn^{2+} cations for fast Zn-ion transport (Figure S18). In addition, the flammability test confirms that the 1,4-BL40 electrolyte inherits the intrinsic safety of aqueous electrolytes (Figure S19). The contact angles between electrolyte and Zn foil decrease from 75.13° to 62.57° when the electrolyte changes from blank to 1,4-BL40. Such enhanced surface wettability facilitates rapid Zn^{2+} migration and uniform distribution (Figure S20).

Therefore, based on the above spectra and theoretical calculations, 1,4-BL40 electrolyte is indeed beneficial to breaking the hydrogen-bond network and manipulating the solvation structure of Zn^{2+}, enhancing the electrochemical performance of SAS@rGO cathode at low temperatures (Figure 5a). SAS@rGO cathode can still maintain a specific capacity of 206 mAh g^{-1} at a current density of 0.2 A g^{-1} and −40 °C, with a considerable capacity retention rate of 79% compared to that at room temperature (Figure 5h). In addition, due to the excellent reaction kinetics of the SAS@rGO cathode and the assistance of the hybrid electrolyte at low temperatures, SAS@rGO can maintain a specific capacity of 150 mAh g^{-1} and a stable cycle for 3000 cycles under a high current density of 1 A g^{-1} (Figure 5i). Such an outstanding electrochemical performance at the low temperature of −40 °C and high current density of 1 A g^{-1} surpasses many other reported low-temperature zinc batteries (Figure 5j).[21,44−48]

In conclusion, a composite cathode (SAS@rGO) was constructed through a straightforward hydrothermal synthesis assisted by host−guest interactions. The designed SAS@rGO electrode exhibits a high specific capacity of ∼360 mAh g^{-1} at 0.2 A g^{-1}, excellent rate performance (capacity retention of 95% at 20 A g^{-1}), and significant long-term cycling stability at low current density (up to 300 cycles with a capacity retention of 90.4% at 0.5 C). This superior electrochemical performance is attributed to the $\pi-\pi$ stacking and hydrogen bond interactions between the SAS and rGO, which confer structural stability to the SAS@rGO during cycling. Furthermore, theoretical calculations and in situ and ex situ characterization demonstrate that SAS@rGO preferentially binds to protons, leading to fast charge storage kinetics. Moreover, the cosolvent 1,4-BL is proposed to disrupt the hydrogen-bond network and manipulate the solvation structure of Zn^{2+}. With the incorporation of 1,4-BL, SAS@rGO achieves stable cycling for 3000 cycles at −40 °C even under a high current density of 1 A g^{-1}, facilitating rapid charge and discharge of aqueous ZIBs at low temperatures.

■ ASSOCIATED CONTENT

Supporting Information

The Supporting Information is available free of charge at https://pubs.acs.org/doi/10.1021/acsenergylett.4c01692.

Experimental details, characterizations, calculations, DFT models, electrochemical measurements, Raman spectra, TG curves, flammability test, the contact angles test and additional electrochemical data (PDF)

■ AUTHOR INFORMATION

Corresponding Authors

Yang Yang − *State Key Laboratory of Physical Chemistry of Solid Surfaces, Collaborative Innovation Center of Chemistry for Energy Materials (iChEM), State-Province Joint Engineering Laboratory of Power Source Technology for New Energy Vehicle, College of Chemistry and Chemical Engineering, Xiamen University, Xiamen 361005, P. R. China*; orcid.org/0000-0003-4215-5767; Email: yangyang419@xmu.edu.cn

Jinbao Zhao − *State Key Laboratory of Physical Chemistry of Solid Surfaces, Collaborative Innovation Center of Chemistry for Energy Materials (iChEM), State-Province Joint Engineering Laboratory of Power Source Technology for New Energy Vehicle, College of Chemistry and Chemical Engineering, Xiamen University, Xiamen 361005, P. R. China*; orcid.org/0000-0002-2753-7508; Email: jbzhao@xmu.edu.cn

Authors

Jin Yang − *State Key Laboratory of Physical Chemistry of Solid Surfaces, Collaborative Innovation Center of Chemistry for Energy Materials (iChEM), State-Province Joint Engineering Laboratory of Power Source Technology for New Energy Vehicle, College of Chemistry and Chemical Engineering, Xiamen University, Xiamen 361005, P. R. China*

Rong Tang − *State Key Laboratory of Physical Chemistry of Solid Surfaces, Collaborative Innovation Center of Chemistry for Energy Materials (iChEM), State-Province Joint Engineering Laboratory of Power Source Technology for New Energy Vehicle, College of Chemistry and Chemical*

https://doi.org/10.1021/acsenergylett.4c01692
ACS Energy Lett. 2024, 9, 4598−4606

Engineering, Xiamen University, Xiamen 361005, P. R. China

Yuanhong Kang − *State Key Laboratory of Physical Chemistry of Solid Surfaces, Collaborative Innovation Center of Chemistry for Energy Materials (iChEM), State-Province Joint Engineering Laboratory of Power Source Technology for New Energy Vehicle, College of Chemistry and Chemical Engineering, Xiamen University, Xiamen 361005, P. R. China*

Minghao Zhang − *State Key Laboratory of Physical Chemistry of Solid Surfaces, Collaborative Innovation Center of Chemistry for Energy Materials (iChEM), State-Province Joint Engineering Laboratory of Power Source Technology for New Energy Vehicle, College of Chemistry and Chemical Engineering, Xiamen University, Xiamen 361005, P. R. China*

Guanhong Chen − *State Key Laboratory of Physical Chemistry of Solid Surfaces, Collaborative Innovation Center of Chemistry for Energy Materials (iChEM), State-Province Joint Engineering Laboratory of Power Source Technology for New Energy Vehicle, College of Chemistry and Chemical Engineering, Xiamen University, Xiamen 361005, P. R. China*

Zeheng Lv − *State Key Laboratory of Physical Chemistry of Solid Surfaces, Collaborative Innovation Center of Chemistry for Energy Materials (iChEM), State-Province Joint Engineering Laboratory of Power Source Technology for New Energy Vehicle, College of Chemistry and Chemical Engineering, Xiamen University, Xiamen 361005, P. R. China*

Zhipeng Wen − *School of Chemical Engineering and Light Industry, Guangdong University of Technology, Guangzhou 510006, P. R. China*

Cheng Chao Li − *School of Chemical Engineering and Light Industry, Guangdong University of Technology, Guangzhou 510006, P. R. China;* orcid.org/0000-0003-2434-760X

Complete contact information is available at: https://pubs.acs.org/10.1021/acsenergylett.4c01692

Notes

The authors declare no competing financial interest.

■ ACKNOWLEDGMENTS

The authors gratefully acknowledge the financial support from National Natural Science Foundation of China (Nos. 22379125, 22109030, and 22021001), Fundamental Research Funds for the Central Universities (20720220073), and Fujian Industrial Technology Development and Application Plan (2022I0002). Numerical computations were performed on Hefei advanced computing center.

■ REFERENCES

(1) Song, M.; Tan, H.; Chao, D.; Fan, H. J. Recent Advances in Zn-Ion Batteries. *Adv. Funct. Mater.* **2018**, *28* (41), No. 1802564.

(2) Ke, J.; Wen, Z.; Yang, Y.; Tang, R.; Tang, Y.; Ye, M.; Liu, X.; Zhang, Y.; Li, C. Tailoring Anion Association Strength Through Polycation-Anion Coordination Mechanism in Imidazole Polymeric Ionic Liquid-Based Artificial Interphase toward Durable Zn Metal Anodes. *Adv. Funct. Mater.* **2023**, *33* (26), No. 2301129.

(3) Song, Y.; Ruan, P.; Mao, C.; Chang, Y.; Wang, L.; Dai, L.; Zhou, P.; Lu, B.; Zhou, J.; He, Z. Metal−Organic Frameworks Functionalized Separators for Robust Aqueous Zinc-Ion Batteries. *Nano-Micro Lett.* **2022**, *14* (1), 218.

(4) Liu, C.; Xie, X.; Lu, B.; Zhou, J.; Liang, S. Electrolyte Strategies toward Better Zinc-Ion Batteries. *ACS Energy Lett.* **2021**, *6* (3), 1015−1033.

(5) Zheng, S.; Wei, L.; Zhang, Z.; Pan, J.; He, J.; Gao, L.; Li, C. In Situ Polymerization of Ionic Liquid with Tunable Phase Separation for Highly Reversible and Ultralong Cycle Life Zn-Ion Battery. *Nano Lett.* **2022**, *22* (22), 9062−9070.

(6) Wang, L.; Zhang, B.; Zhou, W.; Zhao, Z.; Liu, X.; Zhao, R.; Sun, Z.; Li, H.; Wang, X.; Zhang, T.; Jin, H.; Li, W.; Elzatahry, A.; Hassan, Y.; Fan, H. J.; Zhao, D.; Chao, D. Tandem Chemistry with Janus Mesopores Accelerator for Efficient Aqueous Batteries. *J. Am. Chem. Soc.* **2024**, *146* (9), 6199−6208.

(7) Wang, B.; Zhou, W.; Zhang, Y.; Zhang, T.; Li, X.; Feng, Y.; Zhao, R.; Li, W.; Elzatahry, A.; Hassan, Y.; Zhao, D.; Chao, D. An Energetic K+-S Aqueous Battery with 96% Sulfur Redox Utilization. *Joule* **2024**, *8* (7), 2033−2048.

(8) Bu, F.; Sun, Z.; Zhou, W.; Zhang, Y.; Chen, Y.; Ma, B.; Liu, X.; Liang, P.; Zhong, C.; Zhao, R.; Li, H.; Wang, L.; Zhang, T.; Wang, B.; Zhao, Z.; Zhang, J.; Li, W.; Ibrahim, Y. S.; Hassan, Y.; Elzatahry, A.; Chao, D.; Zhao, D. Reviving Zn0 Dendrites to Electroactive Zn2+ by Mesoporous MXene with Active Edge Sites. *J. Am. Chem. Soc.* **2023**, *145* (44), 24284−24293.

(9) Lu, Y.; Cai, Y.; Zhang, Q.; Chen, J. Insights into Redox Processes and Correlated Performance of Organic Carbonyl Electrode Materials in Rechargeable Batteries. *Adv. Mater.* **2022**, *34* (22), No. 2104150.

(10) Tie, Z.; Niu, Z. Design Strategies for High-Performance Aqueous Zn/Organic Batteries. *Angew. Chem., Int. Ed.* **2020**, *59* (48), 21293−21303.

(11) Qin, K.; Huang, J.; Holguin, K.; Luo, C. Recent Advances in Developing Organic Electrode Materials for Multivalent Rechargeable Batteries. *Energy Environ. Sci.* **2020**, *13* (11), 3950−3992.

(12) Gan, X.; Song, Z. Small-Molecule Organic Electrode Materials for Rechargeable Batteries. *Sci. China Chem.* **2023**, *66* (11), 3070−3104.

(13) Cui, H.; Zhu, J.; Zhang, R.; Yang, S.; Li, C.; Wang, Y.; Hou, Y.; Li, Q.; Liang, G.; Zhi, C. Regulating Protons to Tailor the Enol Conversion of Quinone for High-Performance Aqueous Zinc Batteries. *J. Am. Chem. Soc.* **2024**, *146* (22), 15393−15402.

(14) Wang, W.; Balland, V.; Branca, M.; Limoges, B. A Unified Charge Storage Mechanism to Rationalize the Electrochemical Behavior of Quinone-Based Organic Electrodes in Aqueous Rechargeable Batteries. *J. Am. Chem. Soc.* **2024**, *146* (22), 15230−15250.

(15) Zheng, S.; Shi, D.; Yan, D.; Wang, Q.; Sun, T.; Ma, T.; Li, L.; He, D.; Tao, Z.; Chen, J. Orthoquinone−Based Covalent Organic Frameworks with Ordered Channel Structures for Ultrahigh Performance Aqueous Zinc−Organic Batteries. *Angew. Chem.* **2022**, *134* (12), No. e202117511.

(16) Ye, F.; Liu, Q.; Dong, H.; Guan, K.; Chen, Z.; Ju, N.; Hu, L. Organic Zinc-Ion Battery: Planar, π-Conjugated Quinone-Based Polymer Endows Ultrafast Ion Diffusion Kinetics. *Angew. Chem., Int. Ed.* **2022**, *61* (51), No. e202214244.

(17) Liang, Y.; Jing, Y.; Gheytani, S.; Lee, K.-Y.; Liu, P.; Facchetti, A.; Yao, Y. Universal Quinone Electrodes for Long Cycle Life Aqueous Rechargeable Batteries. *Nat. Mater.* **2017**, *16* (8), 841−848.

(18) Sun, Q.; Sun, T.; Du, J.; Li, K.; Xie, H.; Huang, G.; Zhang, X. A Sulfur Heterocyclic Quinone Cathode Towards High-Rate and Long-Cycle Aqueous Zn-Organic Batteries. *Adv. Mater.* **2023**, *35* (22), No. 2301088.

(19) Lin, L.; Lin, Z.; Zhu, J.; Wang, K.; Wu, W.; Qiu, T.; Sun, X. A Semi-Conductive Organic Cathode Material Enabled by Extended Conjugation for Rechargeable Aqueous Zinc Batteries. *Energy Environ. Sci.* **2023**, *16* (1), 89−96.

(20) Shi, R.; Han, C.; Duan, H.; Xu, L.; Zhou, D.; Li, H.; Li, J.; Kang, F.; Li, B.; Wang, G. Redox-Active Organic Sodium Anthraquinone-2-Sulfonate (AQS) Anchored on Reduced Graphene Oxide for High-Performance Supercapacitors. *Adv. Energy Mater.* **2018**, *8* (31), No. 1802088.

(21) Zhang, Q.; Ma, Y.; Lu, Y.; Li, L.; Wan, F.; Zhang, K.; Chen, J. Modulating Electrolyte Structure for Ultralow Temperature Aqueous Zinc Batteries. *Nat. Commun.* **2020**, *11* (1), 4463.
(22) Chang, N.; Li, T.; Li, R.; Wang, S.; Yin, Y.; Zhang, H.; Li, X. An Aqueous Hybrid Electrolyte for Low-Temperature Zinc-Based Energy Storage Devices. *Energy Environ. Sci.* **2020**, *13* (10), 3527−3535.
(23) Wang, R.; Ma, Q.; Zhang, L.; Liu, Z.; Wan, J.; Mao, J.; Li, H.; Zhang, S.; Hao, J.; Zhang, L.; Zhang, C. An Aqueous Electrolyte Regulator for Highly Stable Zinc Anode Under − 35 to 65 °C. *Adv. Energy Mater.* **2023**, *13* (40), No. 2302543.
(24) Ming, F.; Zhu, Y.; Huang, G.; Emwas, A.-H.; Liang, H.; Cui, Y.; Alshareef, H. N. Co-Solvent Electrolyte Engineering for Stable Anode-Free Zinc Metal Batteries. *J. Am. Chem. Soc.* **2022**, *144* (16), 7160−7170.
(25) Lu, T.; Chen, F. Multiwfn: A Multifunctional Wavefunction Analyzer. *J. Comput. Chem.* **2012**, *33* (5), 580−592.
(26) Lu, T.; Chen, Q. Independent Gradient Model Based on Hirshfeld Partition: A New Method for Visual Study of Interactions in Chemical Systems. *J. Comput. Chem.* **2022**, *43* (8), 539−555.
(27) Sun, T.; Li, Z.; Zhi, Y.; Huang, Y.; Fan, H. J.; Zhang, Q. Poly(2,5-Dihydroxy-1,4-Benzoquinonyl Sulfide) As an Efficient Cathode for High-Performance Aqueous Zinc−Organic Batteries. *Adv. Funct. Mater.* **2021**, *31* (16), No. 2010049.
(28) Tie, Z.; Liu, L.; Deng, S.; Zhao, D.; Niu, Z. Proton Insertion Chemistry of a Zinc−Organic Battery. *Angew. Chem., Int. Ed.* **2020**, *59* (12), 4920−4924.
(29) Guo, Z.; Ma, Y.; Dong, X.; Huang, J.; Wang, Y.; Xia, Y. An Environmentally Friendly and Flexible Aqueous Zinc Battery Using an Organic Cathode. *Angew. Chem., Int. Ed.* **2018**, *57*, 11737−11741.
(30) Liu, N.; Wu, X.; Zhang, Y.; Yin, Y.; Sun, C.; Mao, Y.; Fan, L.; Zhang, N. Building High Rate Capability and Ultrastable Dendrite-Free Organic Anode for Rechargeable Aqueous Zinc Batteries. *Adv. Sci.* **2020**, *7* (14), No. 2000146.
(31) Wang, Y.; Wang, C.; Ni, Z.; Gu, Y.; Wang, B.; Guo, Z.; Wang, Z.; Bin, D.; Ma, J.; Wang, Y. Binding Zinc Ions by Carboxyl Groups from Adjacent Molecules toward Long-Life Aqueous Zinc−Organic Batteries. *Adv. Mater.* **2020**, *32* (16), No. 2000338.
(32) Lin, Z.; Shi, H.; Lin, L.; Yang, X.; Wu, W.; Sun, X. A High Capacity Small Molecule Quinone Cathode for Rechargeable Aqueous Zinc-Organic Batteries. *Nat. Commun.* **2021**, *12* (1), 4424.
(33) Chen, Y.; Li, J.; Zhu, Q.; Fan, K.; Cao, Y.; Zhang, G.; Zhang, C.; Gao, Y.; Zou, J.; Zhai, T.; Wang, C. Two-Dimensional Organic Supramolecule via Hydrogen Bonding and $\pi-\pi$ Stacking for Ultrahigh Capacity and Long-Life Aqueous Zinc−Organic Batteries. *Angew. Chem., Int. Ed.* **2022**, *61* (37), No. e202116289.
(34) Zhao, Q.; Huang, W.; Luo, Z.; Liu, L.; Lu, Y.; Li, Y.; Li, L.; Hu, J.; Ma, H.; Chen, J. High-Capacity Aqueous Zinc Batteries Using Sustainable Quinone Electrodes. *Sci. Adv.* **2018**, *4* (3), No. eaao1761.
(35) Ye, Z.; Xie, S.; Cao, Z.; Wang, L.; Xu, D.; Zhang, H.; Matz, J.; Dong, P.; Fang, H.; Shen, J.; Ye, M. High-Rate Aqueous Zinc-Organic Battery Achieved by Lowering HOMO/LUMO of Organic Cathode. *Energy Storage Materials.* **2021**, *37*, 378−386.
(36) Xing, Z.; Xu, G.; Han, J.; Chen, G.; Lu, B.; Liang, S.; Zhou, J. Facing the Capacity Fading of Vanadium-Based Zinc-Ion Batteries. *Trends. chem.* **2023**, *5* (5), 380−392.
(37) Li, C.; Jin, S.; Archer, L. A.; Nazar, L. F. Toward Practical Aqueous Zinc-Ion Batteries for Electrochemical Energy Storage. *Joule.* **2022**, *6* (8), 1733−1738.
(38) Li, S.; Shang, J.; Li, M.; Xu, M.; Zeng, F.; Yin, H.; Tang, Y.; Han, C.; Cheng, H. Design and Synthesis of a π-Conjugated N-Heteroaromatic Material for Aqueous Zinc−Organic Batteries with Ultrahigh Rate and Extremely Long Life. *Adv. Mater.* **2023**, *35*, No. 2207115.
(39) Zhang, Y.; Liang, Y.; Dong, H.; Wang, X.; Yao, Y. Charge Storage Mechanism of a Quinone Polymer Electrode for Zinc-Ion Batteries. *J. Electrochem. Soc.* **2020**, *167* (7), No. 070558.
(40) Xiao, P.; Wu, Y.; Fu, J.; Liang, J.; Zhao, Y.; Ma, Y.; Zhai, T.; Li, H. Enabling High-Rate and High-Areal-Capacity Zn Deposition via an Interfacial Preferentially Adsorbed Molecular Layer. *ACS Energy Lett.* **2023**, *8* (1), 31−39.
(41) Huang, H.; Xie, D.; Zhao, J.; Rao, P.; Choi, W. M.; Davey, K.; Mao, J. Boosting Reversibility and Stability of Zn Anodes via Manipulation of Electrolyte Structure and Interface with Addition of Trace Organic Molecules. *Adv. Energy Mater.* **2022**, *12* (38), No. 2202419.
(42) Brubach, J.-B.; Mermet, A.; Filabozzi, A.; Gerschel, A.; Roy, P. Signatures of the Hydrogen Bonding in the Infrared Bands of Water. *J. Chem. Phys.* **2005**, *122* (18), No. 184509.
(43) Brubach, J.-B.; Mermet, A.; Filabozzi, A.; Gerschel, A.; Lairez, D.; Krafft, M. P.; Roy, P. Dependence of Water Dynamics upon Confinement Size. *J. Phys. Chem. B* **2001**, *105* (2), 430−435.
(44) Dong, Y.; Zhang, N.; Wang, Z.; Li, J.; Ni, Y.; Hu, H.; Cheng, F. Cell-Nucleus Structured Electrolyte for Low-Temperature Aqueous Zinc Batteries. *J. Energy. Chem.* **2023**, *83*, 324−332.
(45) Mo, F.; Liang, G.; Meng, Q.; Liu, Z.; Li, H.; Fan, J.; Zhi, C. A Flexible Rechargeable Aqueous Zinc Manganese-Dioxide Battery Working at − 20 °C. *Energy Environ. Sci.* **2019**, *12* (2), 706−715.
(46) Shen, S.; Ma, D.; Ouyang, K.; Chen, Y.; Yang, M.; Wang, Y.; Sun, S.; Mi, H.; Sun, L.; He, C.; Zhang, P. An In Situ Electrochemical Amorphization Electrode Enables High-Power High-Cryogenic Capacity Aqueous Zinc-Ion Batteries. *Adv. Funct. Mater.* **2023**, *33* (38), No. 2304255.
(47) Zhang, Q.; Xia, K.; Ma, Y.; Lu, Y.; Li, L.; Liang, J.; Chou, S.; Chen, J. Chaotropic Anion and Fast-Kinetics Cathode Enabling Low-Temperature Aqueous Zn Batteries. *ACS Energy Lett.* **2021**, *6* (8), 2704−2712.
(48) Liu, D.; Zhang, Y.; Liu, S.; Wei, L.; You, S.; Chen, D.; Ye, M.; Yang, Y.; Rui, X.; Qin, Y.; Li, C. C. Regulating the Electrolyte Solvation Structure Enables Ultralong Lifespan Vanadium-Based Cathodes with Excellent Low-Temperature Performance. *Adv. Funct. Materials.* **2022**, *32* (24), No. 2111714.

https://doi.org/10.1021/acsenergylett.4c01692
ACS Energy Lett. 2024, 9, 4598−4606